INTERNATIONAL JOURNAL FOR NUMERICAL METHODS IN FLUIDS
Int. J. Numer. Meth. Fluids 0000; **00**:1–20
Published online in Wiley InterScience (www.interscience.wiley.com). DOI: 10.1002/fld

Multi-material closure model for high-order finite element Lagrangian hydrodynamics

V. A. Dobrev[1], Tz. V. Kolev[1], R. N. Rieben[2], V. Z. Tomov[1*]

[1] *Center for Applied Scientific Computing, Lawrence Livermore National Laboratory, Livermore, CA, USA*
[2] *Weapons and Complex Integration, Lawrence Livermore National Laboratory, Livermore, CA, USA*

SUMMARY

We present a new closure model for single fluid, multi-material Lagrangian hydrodynamics and its application to high-order finite element discretizations of these equations [1]. The model is general with respect to the number of materials, dimension, space and time discretization. Knowledge about exact material interfaces is not required. Material indicator functions are evolved by a closure computation at each quadrature point of mixed cells, which can be viewed as a high-order variational generalization of the method of Tipton [2]. This computation is defined by the notion of partial non-instantaneous pressure equilibration, while the full pressure equilibration is achieved by both the closure model and the hydrodynamic motion. Exchange of internal energy between materials is derived through entropy considerations, that is, every material produces positive entropy, and the total entropy production is maximized in compression and minimized in expansion. Results are presented for standard one-dimensional two-material problems, followed by two- and three-dimensional multi-material high-velocity impact arbitrary Lagrangian-Eulerian (ALE) calculations. Copyright © 0000 John Wiley & Sons, Ltd.

Received . . .

KEY WORDS: closure models; pressure equilibration; shock hydrodynamics; multi-material hydrodynamics; finite element methods; high-order methods

1. INTRODUCTION

We are interested in simulating multi-material high-speed flows and shock propagation by solving numerically the Euler equations of compressible hydrodynamics. We are working with Lagrangian methods, where the computational mesh moves with the fluid velocity and we have only a single velocity field to describe the motion of multiple materials. This approach inevitably leads to mesh deterioration, motivating the use of Arbitrary Lagrangian-Eulerian (ALE) methods [3], where the flow field is projected on a better mesh. This produces cells containing multiple materials, meaning that Lagrangian methods must have a mechanism for dealing with such.

*Correspondence to: V. Z. Tomov, Center for Applied Scientific Computing, Lawrence Livermore National Laboratory, 7000 East Ave L-561, Livermore, CA 94550, USA. E-mail: tomov2@llnl.gov

One straightforward approach to define Lagrangian evolution of materials in mixed cells is to say that all materials compress and expand by the same amount, meaning that the volume fractions of all materials stay the same. Stated another way, the volumetric strain of the single velocity field at any point in space is equally partitioned among the multiple materials which may occupy that point in space. This approach can lead to unphysical pressures, as shown for example in [4]. Introducing new variables that control the evolution of volume fractions, however, makes the system underdetermined. The goal of a closure model is to close the Lagrangian system by defining evolution of volume fractions, in a physically reasonable way.

There exist two major closure model approaches. The first one treats a mixed cell as a whole, without reconstructing a sub-cell material interface. A mechanism for equilibration of some quantity is then introduced, usually pressure as in [5], Sections 4.2 and 4.5. Using this equilibration assumption, together with imposition of total volume and energy conservation, methods of this type derive a determined system of equations for the unknown variables in each mixed cell. Another established option is $p + q$ equilibration, where q represents the amount of artificial viscosity in the momentum force, as in the Tipton's method [2]. Descriptions of this method can also be found in [6], Section 3.1, and in [7], Section 7. Other existing options are equal pressure increments as in [8, 4], equal velocity increment as in [5], Section 4.4, equal pressure and equal heat changes (isobar-isoδQ model) as in [9], which has the important property to be entropy-consistent for all materials on fully-discrete level.

The second approach to closure models makes use of material interface reconstruction within mixed cells. Most methods in this category employ of acoustic Riemann solvers in order to predict quantities like interface velocity, material volume changes and pressure. The most recent example is [10], where the authors use that interface information to define pair-wise interactions between materials sharing a common interface. A system of constraints is derived by imposing positivity of volume, positivity of internal energy, and pressure relaxation. This system is solved by an optimization procedure. Other approaches making use of material interfaces can be found in Sections 3.2 and 3.3 in [6], [11], Section 4.6 in [5]. Alternative way to perform a closure computation is presented in [12], where a single-material method is used to evolve total momentum, volume and energy, followed by an intermediate step which distributes those quantities among all materials, then adjusts them by a closure computation, and finally reconstructs the total quantities.

The method developed in this manuscript is motivated by the need for a closure model applicable to high-order finite element discretizations [1], [13]. Because we are not aware of existing methods for reconstructing curvilinear material interfaces for such discretizations, we restrict our closure models to the first of the aforementioned approaches. While there are important differences, e.g. see Section 5, our approach can be viewed as a high-order variational generalization of the method of Tipton [2]. Many of the already existing methods were tested, and while the results were generally acceptable for our low-order discretizations, we could not obtain satisfactory results with higher degree polynomials. Existing closure models are exclusively designed for staggered-grid hydrodynamics (SGH) discretizations. In SGH, a mixed cell evolves a single volume fraction value for each material. In our case, however, a mixed cell must evolve each material's volume fraction at a set of quadrature points. This leads to different accelerations at the different quadrature points, resulting in waves traveling across the mixed cell. Compared to the classic SGH case, closure models for high-order methods require extra robustness.

DOI: 10.1002/fld

This paper presents a new closure model that is compatible with high-order finite element discretizations. The model is defined on continuous level, which makes it independent of dimension, space and time discretization. The method achieves sub-cell resolution without any knowledge of explicit material interfaces. Volume fractions are represented as general functions (material indicator functions), and evolved at each integration point by a partial non-instantaneous pressure equilibration procedure. The full pressure equilibration is achieved by the combined action of the closure model and hydrodynamic motion. Each material-specific internal energy equation uses its own material's pressure, and an energy exchange term is introduced to account for the volume fraction changes. This internal energy exchange is determined so that every material produces positive entropy, and the total entropy production is maximized in compression and minimized in expansion. The model itself introduces two extra parameters, that is, rate of equilibration and maximum indicator change within a time step. We present computational tests for standard one-, two- and three-dimensional problems, resulting from the implementation of the proposed closure model in the framework of [1].

The remainder of this manuscript has the following organization. In Section 2 we review the underlying high-order finite element framework. Volume fractions are represented as continuous functions and the resulting continuous multi-material Lagrangian system is derived in Section 3. The discrete representation of multi-material quantities is presented in Section 4. In Section 5 we present the details of the closure model. Finally, in Section 6 we present numerical results on a set of 1D, 2D and 3D benchmark problems.

2. PRELIMINARIES

This work builds on top of an existing single-material Lagrangian method. In this section we briefly go over the underlying finite element framework; the complete description can be found in [1].

Let $\hat{\Omega}$ be the initial domain. Material velocity v and mesh position x are discretized in the finite element space $\mathcal{V} \subset [H^1(\hat{\Omega})]^d$, with basis $\{w_i\}$. Specific internal energy e is discretized in $\mathcal{E} \subset L_2(\hat{\Omega})$, with basis $\{\phi_j\}$. Throughout this manuscript we refer to the pairs of spaces $Q_k Q_{k-1}$, by which we denote $\mathcal{V} = (Q_k)^d$, i.e., the Cartesian product of the space of continuous finite elements on quadrilateral or hexahedral meshes of degree k, and $\mathcal{E} = \hat{Q}_k$, the companion space of discontinuous finite elements of order one less than the kinematic space. The density ρ is computed point-wise from the transformation to the initial positions, namely, for a point $x(\hat{x}, t)$ we compute $\rho(x) = \rho_0(\hat{x})/|J(\hat{x}, t)|$. Our semi-discrete formulation uses the mass matrices $\boldsymbol{M}_{\mathcal{V}}, \boldsymbol{M}_{\mathcal{E}}$, and the force matrix $\boldsymbol{F}$, which are defined as

$$(\boldsymbol{M}_{\mathcal{V}})_{ij} = \int_{\Omega(t)} \rho w_j w_i \,, \qquad (\boldsymbol{M}_{\mathcal{E}})_{ij} = \int_{\Omega(t)} \rho \phi_j \phi_i \,, \qquad \boldsymbol{F}_{ij} = \int_{\Omega(t)} (\sigma : \nabla w_i) \phi_j \,. \tag{1}$$

Here $\sigma = -pI + \sigma_a$ is a general stress tensor that includes artificial viscosity stresses; for the particular expression and viscosity coefficients we refer to [1], Section 6. The resulting semi-discrete form is

$$\boldsymbol{M}_{\mathcal{V}} \frac{d\boldsymbol{v}}{dt} = -\boldsymbol{F} \cdot \boldsymbol{1} \,, \qquad \boldsymbol{M}_{\mathcal{E}} \frac{d\boldsymbol{e}}{dt} = \boldsymbol{F}^T \cdot \boldsymbol{v} \,, \qquad \frac{d\boldsymbol{x}}{dt} = \boldsymbol{v} \,. \tag{2}$$

Prepared using fldauth.cls
DOI: 10.1002/fld

In this work we also refer to the point-wise, direction-dependent length scale h that is explained in detail in [1], Section 6.3. The semi-discrete system (2) is discretized in time by standard explicit high-order time integration techniques, e.g., explicit Runge-Kutta methods.

3. CONTINUOUS MULTI-MATERIAL LAGRANGIAN SYSTEM

In this section we define the representation of different materials and derive the governing equations for their evolution on continuous level. All referred quantities depend on time, but for ease of notation we skip the time parameter t. Consider some domain Ω with volume V. It contains multiple materials with volumes V_k, where $k = 1 \dots N$ is the material index, s.t. $\sum_k V_k = V$. The material indicator functions $\eta_k(x)$ are defined by the requirement that

$$V_k(U) = \int_U \eta_k(x) \tag{3}$$

for any subdomain $U \subset \Omega$, where $V_k(U)$ is the volume of the kth material contained in U, i.e. $\{\eta_k\}$ are the densities corresponding to material volumes. Let $V(U) = |U|$ be the volume of the subdomain U, then the pointwise volume fraction at a fixed point $x \in \Omega$, can be defined as

$$\frac{V_k(x)}{V(x)} := \lim_{\epsilon \to 0} \frac{V_k(B_\epsilon)}{V(B_\epsilon)}\,, \tag{4}$$

where B_ϵ is a ball of radius ϵ around x. By the definition and the continuity of $\eta_k(x)$, it follows that these functions can also be viewed as the point-wise volume fractions:

$$\eta_k(x) = \lim_{\epsilon \to 0} \frac{\int_{B_\epsilon} \eta_k}{|B_\epsilon|} = \frac{V_k(x)}{V(x)}\,. \tag{5}$$

Using the same limiting approach and the Reynolds transport theorem, we can derive the standard equation for the rate of change of V, namely,

$$\frac{1}{V(x)}\frac{dV(x)}{dt} = \lim_{\epsilon \to 0} \frac{1}{|B_\epsilon|}\frac{d}{dt}\int_{B_\epsilon} 1 = \lim_{\epsilon \to 0} \frac{1}{|B_\epsilon|}\int_{B_\epsilon} \nabla \cdot v = (\nabla \cdot v)(x)\,,$$

leading to the point-wise equation

$$\frac{1}{V}\frac{dV}{dt} = \nabla \cdot v\,. \tag{6}$$

This and (5) can be combined to obtain

$$\frac{1}{V}\frac{dV_k}{dt} = \frac{d\eta_k}{dt} + \eta_k \nabla \cdot v\,. \tag{7}$$

In general, each material should move with its own velocity. However, in the single fluid framework considered in this paper, only one common velocity is used for all materials. To approximately represent the divergence of the unknown velocity of each material, we introduce the quantity

$$d_k := \frac{1}{V_k}\frac{dV_k}{dt}\,. \tag{8}$$

Prepared using fldauth.cls
DOI: 10.1002/fld

At points where $\nabla \cdot v \neq 0$, this quantity is related to the commonly used relative material volume change (or volumetric strain) $\beta_k := \frac{dV_k(x)}{dV(x)}$, see e.g. [4], through the equation

$$\beta_k \nabla \cdot v = \eta_k d_k \,. \tag{9}$$

Combining (8) with (7) results in the evolution equation for η_k:

$$\frac{d\eta_k}{dt} = \eta_k (d_k - \nabla \cdot v) =: \alpha_k \,. \tag{10}$$

By the definitions of η_k and α_k,

$$\sum_k \eta_k = 1 \quad \text{and} \quad \sum_k \alpha_k = \sum_k \frac{d\eta_k}{dt} = 0 \,.$$

The quantity α_k is of central importance in closure models, since it controls the rate of volume redistribution between materials. Different choices of α_k correspond to different closure models, but every choice of α_k must satisfy $\sum_k \alpha_k = 0$. The special case of $\alpha_k = 0$, or equivalently $d_k = \nabla \cdot v$, corresponds to η_k being Lagrangian, i.e., each mixed region would keep its material indicator functions constant. There is no equation for α_k; formulas for it are derived by imposing physical considerations, e.g., pressure equilibration between materials, see Section 5.

Next we turn our attention to the material-specific density and internal energy. In the above spirit we define material density $\rho_k(x)$ and specific internal energy $e_k(x)$ through the material mass M_k and material internal energy IE_k in subdomains $U \subseteq \Omega$, namely,

$$M_k(U) = \int_U \eta_k \rho_k \,, \quad IE_k(U) = \int_U \eta_k \rho_k e_k \,.$$

Taking limits, as in (5), leads to the point-wise expressions

$$\eta_k(x)\rho_k(x) = \frac{M_k(x)}{V(x)} \,, \quad \eta_k(x)\rho_k(x)e_k(x) = \frac{IE_k(x)}{V(x)} \,. \tag{11}$$

The total density ρ and internal specific energy e are defined analogously, based on the total mass M and the total internal energy IE. Using the facts that $M = \sum_k M_k$ and $IE = \sum_k IE_k$ together with (11), we have

$$\rho = \sum_k \eta_k \rho_k \,, \quad \rho\, e = \sum_k \eta_k \rho_k e_k \,. \tag{12}$$

The Lagrangian frame property that no mass travels through the mesh, i.e. $dM_k(x)/dt = 0$, combined with (11) and (6), gives the evolution equation for material mass, namely,

$$\frac{d(\eta_k \rho_k)}{dt} = -\eta_k \rho_k \nabla \cdot v. \tag{13}$$

Note that due to (10), this is equivalent with

$$\frac{d\rho_k}{dt} = -\rho_k d_k \,, \tag{14}$$

DOI: 10.1002/fld

which looks exactly as the standard mass conservation equation in the single-material case with ρ replaced by ρ_k and $\nabla \cdot v$ replaced by d_k.

As for the material-dependent specific internal energy equations, it is natural to start with

$$\frac{dIE_k(x)}{dt} = -p_k \frac{dV_k}{dt} \,.$$

The left-hand side is expressed by (11), and the right-hand side by (7) and (10), resulting in

$$\eta_k \rho_k \frac{de_k}{dt} = -\eta_k p_k d_k \,. \tag{15}$$

To get total energy conservation in the single-fluid formulation, the right-hand sides in (15) need to sum to $p\nabla \cdot v$, where p is the total pressure (still to be defined) used in the momentum equation:

$$\sum_k \eta_k p_k d_k = p \nabla \cdot v \,.$$

Since

$$\eta_k p_k d_k = \eta_k p_k \nabla \cdot v + \eta_k p_k (d_k - \nabla \cdot v) = \eta_k p_k \nabla \cdot v + p_k \alpha_k \,,$$

and since $\sum_k \alpha_k = 0$, one natural way to obtain total energy conservation is to define the total pressure as $p = \sum_k \eta_k p_k$ and to replace p_k in the second (perturbation) term above with a pressure $\bar{p}$ that is common for all materials, see Section 5:

$$\eta_k \rho_k \frac{de_k}{dt} = -\eta_k p_k \nabla \cdot v - \bar{p} \alpha_k \,. \tag{16}$$

Equation 16 reduces to (15) when $\bar{p} = p_k$, i.e., when pressures are in equilibrium or there is only one material at the point, in which case $\alpha_k = 0$. Since the second term on the right-hand side of (16) sums to zero over materials, it can be viewed as redistribution of internal energy due to interaction between materials.

The final multi-material Lagrangian system becomes

$$\frac{d\eta_k}{dt} = \alpha_k \,, \tag{17}$$

$$\frac{d(\eta_k \rho_k)}{dt} = -\eta_k \rho_k \nabla \cdot v \,, \tag{18}$$

$$\rho \frac{dv}{dt} = \nabla \cdot \sum_k \eta_k \sigma_k \,, \tag{19}$$

$$\eta_k \rho_k \frac{de_k}{dt} = \eta_k \sigma_k : \nabla v - \bar{p} \alpha_k \,, \tag{20}$$

with $\sigma_k = -p_k I + \sigma_{a,k}$, where $\sigma_{a,k}$ is the artificial viscosity stress tensor. It is the closure model's task to define the extra $N + 1$ variables $\{\alpha_k\}$ and $\bar{p}$.

Remark 1

Note that we use the so-called "gathering approach", i.e., artificial viscosity is computed for each material and used in the corresponding internal energy equation with η_k scaling. All material

DOI: 10.1002/fld

viscosities sum to form the total momentum viscosity. Alternative to this is the "distribution approach", see Section 3.2 in [10].

4. DISCRETIZATION DETAILS

In discretizing the system (17)–(20) we mostly follow the existing single material approach, namely, in space we use high-order finite elements for $x, v, \{e_k\}$, and in time we apply a generic high-order explicit time integration. The material-specific masses $\eta_k \rho_k$ are evolved in a discrete set of points using the transformation to the initial positions, i.e., for a point $x = x(\hat{x}, t)$ we have $\eta_k(x,t)\rho_k(x,t) = \eta_{k0}(\hat{x})\rho_{k0}(\hat{x})/|J(\hat{x},t)|$.

The newly introduced variables η_k are also evolved point-wise, based on (17). The points of interest are the ones at which the values of $\{\eta_k\}, \{\alpha_k\}$ and $\bar{p}$ are needed, namely, the quadrature points used to evaluate the integrals on the right-hand sides of (19) and (20). Originally, we considered the use of a finite element representation of η_k; however some numerical experiments suggested that the transition between finite element degrees of freedom and quadrature points (through L_2 projection) introduced undesirable pressure oscillations in the closure computation.

Initialization in mixed cells Since the proposed method does not require interface knowledge, at each point within a mixed cell we require $\eta_k > 0$ (to prevent infinite density), $\sum_k \eta_k = 1$, well-defined ρ_k and e_k throughout the cell, and correct material pressures p_k.

The initialization of η_k is carried out in two steps. First, the initial jump of each η_k is approximated by a finite element function in the positive Bernstein basis:

$$\eta_k(x, t=0) = \begin{cases} 1 & \text{if material } k \text{ is present at } x \\ 0 & \text{otherwise} \end{cases} \tag{21}$$

Second, these finite element functions are interpolated at the quadrature points of interest, by which the initial indicator values are obtained. The utilization of the positive Bernstein basis results in a smooth transition between 0 and 1 within the mixed cell. Note that this procedure might introduce an initial volume error for more complicated interfaces that are not aligned with the finite element degrees of freedom within the cell.

The material specific densities and internal energies are initialized according to

$$\rho_k(x, t=0) = \begin{cases} \rho(x,0)|_k & \eta_k(x,0) > 0\,, \\ 0 & \eta_k(x,0) = 0\,, \end{cases} \qquad e_k(x, t=0) = \begin{cases} e(x,0)|_k & \eta_k(x,0) > 0\,, \\ 0 & \eta_k(x,0) = 0\,. \end{cases} \tag{22}$$

Here $\rho|_k$ and $e|_k$ provide additional values for material k in mixed cells, at points where the material's values are not defined by the initial conditions, i.e., $\rho|_k$ and $e|_k$ extend the initial conditions for material k wherever $\eta_k(x,0) > 0$. The aim of these extensions is to define the material-dependent quantities throughout the whole cell and obtain pressures that agree with the initial conditions.

Prepared using fldauth.cls
DOI: 10.1002/fld

Example of initialization between two materials in 1D is shown in Figure 1. Presented is a mixed cell in $[0.5, 0.55]$ with an interface at $x = 0.525$. The initial condition is $\rho_L = 0.8, \rho_R = 0.2, p_L = 2.0, p_R = 0.1$. The chosen finite element spaces (Q_4Q_3 pair) result in 8 quadrature points of interest. Note that this initialization results in correct initial material pressures and smooth total pressure.

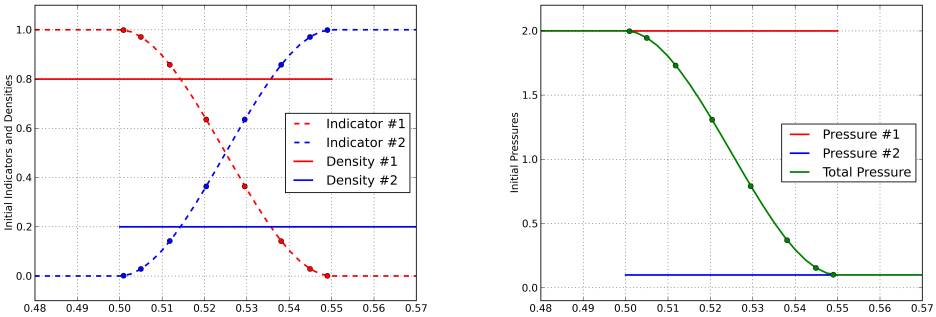

Figure 1. Initialization of material-specific quantities in 1D. Left panel: Material indicators and densities. Right panel: Material pressures and total pressure. Solid dots correspond to values at quadrature points of interest.

Evolution and limiting of η_k The time integration of (17) follows the general high order algorithm at each point of interest. That is, in a Runge-Kutta time integration sub-stage with a time step $c\Delta t$, we update η_k at each point by

$$\eta_k^* = \eta_k + c\Delta t \alpha_k \,. \tag{23}$$

Here α_k is computed by the closure model, and all other quantities on the right-hand side are explicit. This is done for mixed points, i.e., integration points in cells that are mixed. Note that we retain the partition of unity property, $\sum_k \eta_k^* = 1$, since $\sum_k \alpha_k = 0$.

Big sudden changes in material indicators might lead to oscillations in density or energy. Therefore, the increments α_k are limited whenever

$$|c\Delta t \alpha_k| > c_L \eta_k \,,$$

where $c_L \in (0, 1)$ is the maximum indicator change ratio. In this case we first modify these values to be

$$\alpha_k^* = \operatorname{sign}(\alpha_k) \frac{c_L \eta_k}{c\Delta t} \,.$$

Since $\sum_k \alpha_k^* = 0$ does not hold after this change, we apply additional scaling to restore the zero sum. Specifically, we consider $A^+ = \sum_{\alpha_k^* > 0} \alpha_k^*$ and $A^- = \sum_{\alpha_k^* < 0} \alpha_k^*$, and compute

$$\alpha_k' = \begin{cases} -\frac{A^-}{A^+} \alpha_k^* & \text{if } \alpha_k^* > 0 \text{ and } A^+ + A^- > 0 \,, \\ -\frac{A^+}{A^-} \alpha_k^* & \text{if } \alpha_k^* < 0 \text{ and } A^+ + A^- < 0 \,, \\ \alpha_k^* & \text{otherwise} \,. \end{cases}$$

DOI: 10.1002/fld

These adjusted increments satisfy $\sum_k \alpha'_k = 0$ and $|c\Delta t\alpha'_k| \leq c_L\eta_k$ (the latter holds since $|\alpha'_k| \leq |\alpha^*_k|$). Finally, (23) is replaced by

$$\eta^*_k = \eta_k + c\Delta t\alpha'_k \,. \tag{24}$$

Here $\eta^*_k > 0$ since $c_L < 1$. Also $\eta^*_k < 1$ since $\sum_k \eta^*_k = 1$. Furthermore, the evaluation of the right-hand side of (20) uses α'_k instead of the original values α_k.

5. CLOSURE MODEL

In this section we describe our method for calculating the quantities $\{\alpha_k\}$ and $\bar{p}$ at the integration points used for evaluating the right-hand sides of (17), (20). For ease of notation we suppress most of the time superscripts.

Definition of $\boldsymbol{\alpha_k}$ An estimate for the future pressure is obtained by the equation $dp_k = -\kappa_k dV_k/V_k$ where $\kappa_k = \rho_k C^2_{s,k}$ is material k's bulk modulus, and $C_{s,k}$ is the sound speed of material k. Using (8), this can be written as

$$\frac{dp_k}{dt} = -\kappa_k d_k \,. \tag{25}$$

Then a fully-discrete approximation of the expected pressure at a quadrature point, after a time step τ, is

$$p'_k = p^n_k - \tau\kappa_k d_k = p^n_k - \tau\kappa_k \nabla\cdot v - \tau\kappa_k \frac{\alpha_k}{\eta_k} \,. \tag{26}$$

The last term above corresponds to the closure contribution to the pressure update.

Pressure equilibration implies (26) to be independent of k. The closure model we present targets the equilibration of the first and third terms, i.e., its goal is to have the quantity

$$p^* = p^n_k - \tau\frac{\kappa_k}{\eta_k}\alpha_k \tag{27}$$

independent of k. The term $\tau\kappa_k\nabla\cdot v$ is left to the hydrodynamic motion, namely, $\nabla\cdot v \to 0$ in the absence of shocks and external forces. The full relaxation of the material pressures results from the combined action of the closure model and the dynamics of the system.

The N equations (27), together with $\sum_k \alpha_k = 0$, provide a determined system for the $N+1$ unknowns $\{\alpha_k\}$ and p^*. Its solution is

$$p^* = \sum_k \left(p_k \frac{\eta_k}{\kappa_k}\right) \Big/ \left(\sum_k \frac{\eta_k}{\kappa_k}\right) \,, \tag{28}$$

$$\alpha_k = \frac{1}{\tau}(p_k - p^*)\frac{\eta_k}{\kappa_k} \,. \tag{29}$$

These quantities are evaluated for mixed cells, at the integration points that are used to compute the integrals resulting from the Galerkin discretization of (19) and (20). One important consequence of (29) is that every expanding material ($\alpha_k > 0$) has a higher pressure than every compressing

DOI: 10.1002/fld

material ($\alpha_k < 0$). This allows a definition of energy exchange, later in this section, which is entropy-consistent for every material.

The time scale τ is defined at each integration point by

$$\tau = c_\tau \max_k \left(\frac{h}{C_{s,k}} \right) , \tag{30}$$

where c_τ is an adjustable constant. A way to define a mixed sound speed, which accounts for material pressure differences, is presented in [10], Section 4.5, and can also be applied in the definition of τ. The formula (30), however, implies that τ is bigger than (or at least very close to) the actual global computational time step Δt, see [1], Section 7.3. Therefore, the above procedure does not enforce instantaneous equilibration. Each point computes its equilibrium value and relaxes its material pressures towards that value. Decreasing c_τ leads to faster pressure relaxation, but setting the value too small makes the method unstable.

Definition of common force There are different options to define the common force in the momentum equation. We do not define it through p^*, because the equilibration is not instantaneous, and we must take into account that the material pressures are in general different. The two most common remaining options are

$$p = \sum_k \eta_k p_k^n , \qquad p = \sum_k \eta_k p_k' .$$

They can be seen as explicit and implicit, respectively. The explicit one is chosen, because it does not require changing our existing single-material algorithms. It has also proven slightly more stable in our tests. Total energy conservation is then achieved by writing the internal energy equation as in (16).

Definition of energy exchange Recall the final form of the material density and specific internal energy equations:

$$\eta_k \frac{d\rho_k}{dt} = -\eta_k \rho_k d_k = -\eta_k \rho_k \nabla \cdot v - \rho_k \alpha_k , \tag{31}$$

$$\eta_k \rho_k \frac{de_k}{dt} = -\eta_k p_k \nabla \cdot v - \bar{p} \alpha_k + \mathcal{V}_k , \tag{32}$$

where $\mathcal{V}_k$ is a positive viscosity term. Next we derive an expression for $\bar{p}$.

Consider the specific entropy for material k, $s_k(\rho_k, e_k)$, defined through the thermodynamic identity

$$T_k ds_k = de_k + p_k d\left(\frac{1}{\rho_k} \right) , \tag{33}$$

and its derivatives

$$\frac{\partial s_k}{\partial e_k} = \frac{1}{T_k} , \quad \frac{\partial s_k}{\partial \rho_k} = -\frac{p_k}{T_k \rho_k^2} . \tag{34}$$

Note that

$$p_k \frac{\partial s_k}{\partial e_k} + \rho_k^2 \frac{\partial s_k}{\partial \rho_k} = 0 . \tag{35}$$

DOI: 10.1002/fld

Equation for s_k is derived by multiplying (31) by $\rho_k \frac{\partial s_k}{\partial \rho_k}$, (32) by $\frac{\partial s_k}{\partial e_k}$, and adding the resulting equations:

$$\eta_k \rho_k \frac{ds_k}{dt} = -\nabla \cdot v \eta_k \left(\rho_k^2 \frac{\partial s_k}{\partial \rho_k} + p_k \frac{\partial s_k}{\partial e_k} \right) - \alpha_k \left(\rho_k^2 \frac{\partial s_k}{\partial \rho_k} + \bar{p} \frac{\partial s_k}{\partial e_k} \right) + \frac{1}{T_k} \mathcal{V}_k \quad \Rightarrow \tag{36}$$

$$\eta_k \rho_k \frac{ds_k}{dt} = \frac{\alpha_k}{T_k}(p_k - \bar{p}) + \frac{1}{T_k} \mathcal{V}_k \,. \tag{37}$$

To be consistent with the entropy inequality (second law of thermodynamics), the right-hand side must be positive. The viscosity term is positive by construction. The first term on the right-hand side accounts for the k-th material's entropy change due to the closure model. Ideally, we want this term to be positive for all k. Therefore, $\bar{p}$ can be bounded as:

$$\max_{k-}(p_k) \leq \bar{p} \leq \min_{k+}(p_k) \,, \tag{38}$$

where $k+$ are the indices of the expanding materials ($\alpha_k > 0$), and $k-$ are the indices of the compressing materials ($\alpha_k < 0$). Having $\bar{p}$ within these bounds, guarantees that the closure model provides positive entropy production for all materials. Note that the inequality (38) defines a non-empty interval, because (29) guarantees that all expanding materials have higher pressures than all compressing materials.

The final value from this interval is determined by trying to reproduce the physical behavior of the entropy, namely, the fact that entropy production is large in compression, and small in expansion. Therefore, two cases are considered. In compression, i.e., $\nabla \cdot v < 0$, $\bar{p}$ is chosen to maximize the quantity, $\sum_k T_k \frac{ds_k}{dt}$. In expansion, i.e., $\nabla \cdot v > 0$, $\bar{p}$ is chosen to minimize that quantity. Note that T_k is included in the sum in order to avoid divisions by T_k, which can cause instabilities for small energies. Because the total entropy change is a linear function of $\bar{p}$, its extreme values are at $\min_{k+}(p_k)$ and $\max_{k-}(p_k)$, namely,

$$\bar{p} = \begin{cases} \underset{p \in \{\max_{k-}(p_k), \min_{k+}(p_k)\}}{\operatorname{argmax}} \sum_k \frac{\alpha_k}{\eta_k \rho_k}(p_k - p) \,, & \text{if } \nabla \cdot v \leq 0 \,, \\ \underset{p \in \{\max_{k-}(p_k), \min_{k+}(p_k)\}}{\operatorname{argmin}} \sum_k \frac{\alpha_k}{\eta_k \rho_k}(p_k - p) \,, & \text{if } \nabla \cdot v > 0 \,. \end{cases} \tag{39}$$

Remark 2
In (37), it is interesting to note that using constant volume fractions, i.e. $\alpha_k = 0$, is in agreement with the second law.

6. NUMERICAL TESTS

In this section we present results in the context of standard closure model benchmarks existing in the literature. We begin by considering 1D purely Lagrangian calculations with two materials and one mixed cell. For these tests, the presentation focuses on the time evolution of $\{\eta_k, \rho_k, e_k, p_k\}$ at the mixed quadrature points. Pure cell computations are used as reference solutions. Next, 2D and 3D high velocity impact ALE simulation are presented. These problems contain three materials

Prepared using fldauth.cls
DOI: 10.1002/fld

and develop many mixed cells. For the ALE tests, the presentation focuses on the general material evolution and the robustness of the closure model.

The remesh and multi-material remap phases of the high-order finite element framework [1] will be presented in a future publication. For the purposes of this presentation, it is sufficient to know that our remap is advection based and does not involve interface reconstruction. Furthermore, each material indicator is remapped by projecting its quadrature point values to a finite element function, remapping this function to the new mesh, and interpolating the result back at the quadrature points of interest. The remap preserves the starting maximum and minimum values of all fields $\{\eta_k, \rho_k, e_k\}$ and retains $\sum_k \eta_k = 1$.

All presented simulations use the parameters $c_L = 0.05$ and $c_\tau = 0.25$. Time integration is performed by the RK2-average method as described in [1], Section 7, where both steps are extended with the material indicators update (23). All physical units in this section are based on the $(cm, g, \mu s)$ unit system, which means velocities are in $\frac{cm}{\mu s}$, densities are in $\frac{g}{cm^3}$ and stresses are in $Mbar$. The results were generated using the BLAST code [14].

6.1. Incoming Shock

The first result we present is a simple 1D simulation of a shock compressing an equilibrated interface. This test problem illustrates the deficiencies associated with treating the material indicator functions as Lagrangian quantities , i.e., $\alpha_k = 0$, and the ability of the closure model to respond to incoming shocks.

The following setup is used: The domain is $x \in [0, 100]$ with two materials. The right boundary is "wall" while a constant velocity source of $v = 1$ is applied to the boundary $x = 0$, i.e., a piston with constant velocity, which launches a shock from $x = 0$, compressing each material. Both materials are initialized with the same pressure $p_1 = p_2 = 0.1$. The left side of the domain consists of material 1, a gamma law gas with $\gamma_1 = 4.0$ and initial density $\rho_1 = 0.1$. The right side of the domain consists of material 2, a gamma law gas with $\gamma_2 = 5/3$ and initial density $\rho_2 = 1.0$. Material 1 therefore has a bulk modulus of $\kappa_1 = \gamma_1 p_1 = 0.4$ and material 2 initially has a bulk modulus of $\kappa_2 = \gamma_2 p_2 = 0.16666$. Material 1 is less compressible than material 2, i.e. for a given total volume change associated with a point, we expect material 1 to change its volume less than material 2 does (i.e., material 1 should expand relative to material 2). The problem is run to a final time of $t = 25$ and requires artificial viscosity. Presented is a Q_1Q_0 discretization on 200 cells with an interface between the two materials at $x = 50$ for the pure simulation, and $x = 50.25$ for the mixed cell simulations.

The final total pressure, density and specific internal energy are shown on Figure 2. The material interface at final time is around $x = 57$. Figure 3 shows the time evolution of the mixed cell for the material specific pressures, densities, specific internal energies, and indicator functions. The plot compares the pure cells simulation to (1) mixed simulation done with an active closure model and (2) mixed simulation done with Lagrangian indicators. It is clear in this figure that the closure model is essential to reproducing the pure results for all fields. The presented model produces the expected physical behavior and obtains accurate values for all fields.

Prepared using fldauth.cls
DOI: 10.1002/fld

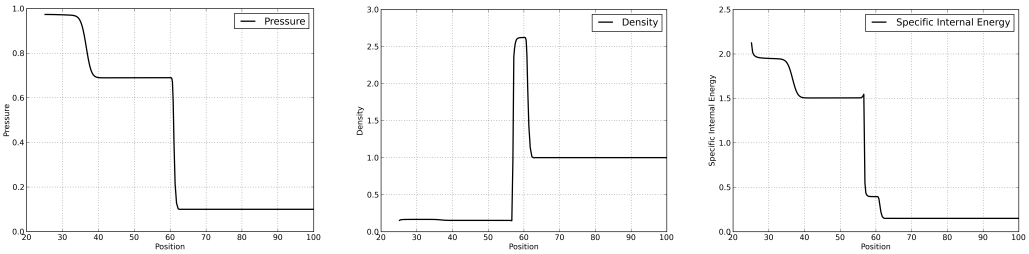

Figure 2. Total pressure, density and specific internal energy at $t = 25$ for the incoming shock test.

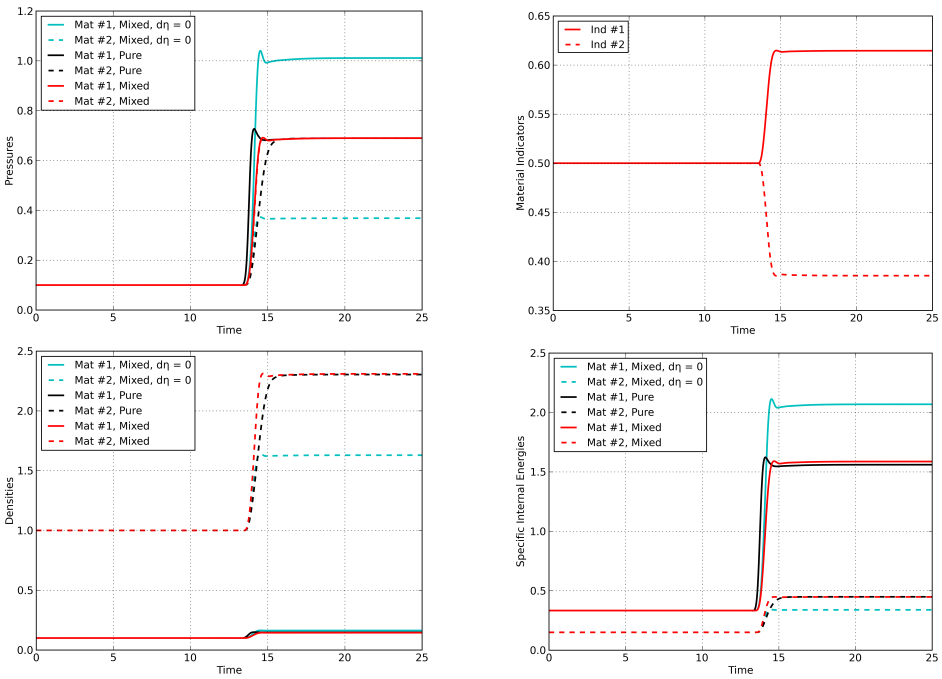

Figure 3. Time evolution of the mixed cell for the incoming shock test.

6.2. *Two-Material Sod Tube*

Next we consider the 1D two-material Riemann problem introduced in [15]. This problem tests the ability of the method to deal with a pressure discontinuity at initial time. We begin by presenting a Q_1Q_0 discretization, and then present a higher-order Q_3Q_2 discretization with 5 integration points in the mixed cell.

The domain is $x \in [0, 1]$ with $v(0) = v(1) = 0$ boundary conditions. Both materials are ideal gases with EOS $p = (\gamma - 1)\rho e$. The interface is at $x_i = 0.5$ for the pure simulations, and is moved to $x_i = 0.5 + 0.5h$ for the mixed cell simulations. The problem is run to a final time of $t = 0.2$. The two initial states are

$$(v, \rho, e, p, \gamma) = \begin{cases} (0, 1, 2, 2, 2) & \text{if } x < x_i \text{ (Material \#1)}, \\ (0, 0.125, 2, 0.1, 1.4) & \text{if } x > x_i \text{ (Material \#2)}. \end{cases}$$

To confirm that the current closure model is consistent with the previously presented results [9, 16, 6, 12, 5, 10], we perform a Q_1Q_0 simulation on 100 cells. In this case, for the mixed

DOI: 10.1002/fld

simulation, closure model is computed at one quadrature point. The final total pressure, density and specific internal energy from the mixed simulation are shown on Figure 4. Figure 5 shows the time evolution of the mixed cell for the material specific pressures, indicator functions, densities and specific internal energies. The plot compares the pure cells simulation to the mixed cell simulation. All fields behave as expected.

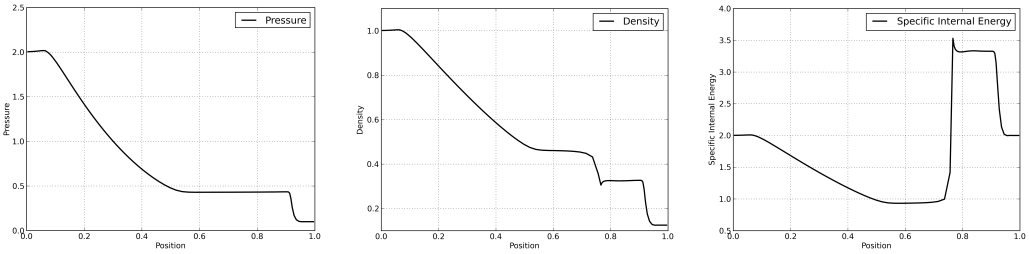

Figure 4. Total pressure, density and specific internal energy at $t = 0.2$ for the two-material Sod tube test.

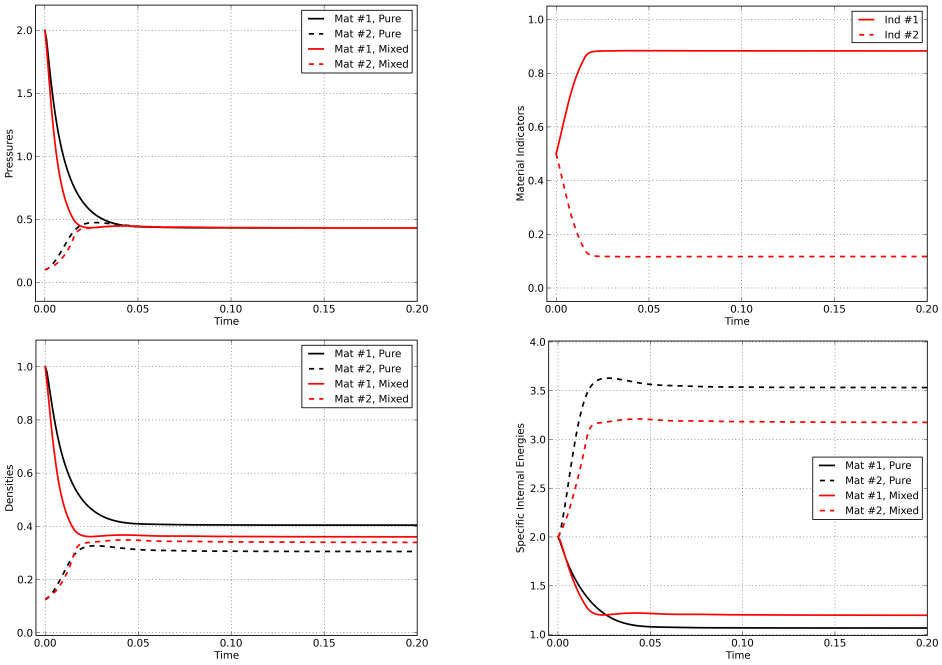

Figure 5. Time evolution of the mixed point for the Q_1Q_0 two-material Sod tube test.

Next a Q_3Q_2 test is performed on 20 cells. The closure model is evaluated at 5 distinct quadrature points within the mixed cell. Figure 6 tracks time evolution around the interface for both Q_3Q_2 pure and mixed cell simulations. This plot compares (i) the left-most, middle, and right-most quadrature points of the mixed cell to the (ii) closest to the interface quadrature points of the pure cells. Pressure equilibration is achieved at every quadrature point with few oscillations. As expected, the left material pushes away the right material at every quadrature point, until equilibrium is achieved. A jump in pressure appears for material 2's left-most point, where the already small material indicator is additionally compressed. This jump is well distributed between its density and specific internal energy. This is an important feature for the robustness of the simulation. In particular, there are no big energy spikes that can affect the simulation time step.

DOI: 10.1002/fld

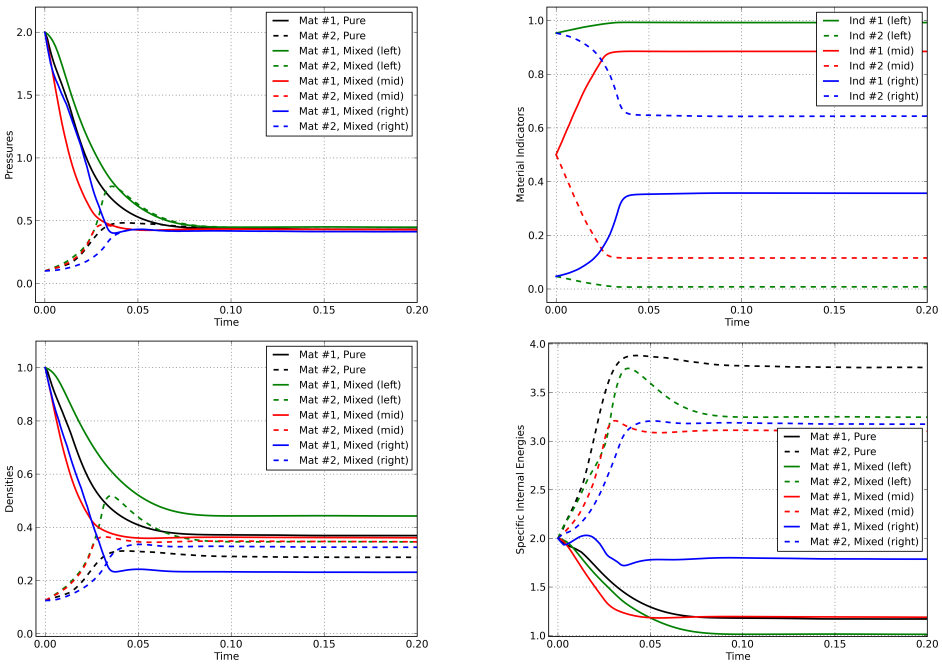

Figure 6. Time evolution of the mixed points for the Q_3Q_2 two-material Sod tube test.

6.3. *Water-Air Shock Tube*

The next test is a more severe 1D Riemann problem. It represents a water-air interaction with big initial pressure jump. This problem tests the robustness of the high-order closure model.

The domain is $x \in [0, 1]$ with $v(0) = v(1) = 0$ boundary conditions. The left material is modeled by the stiffened-gas EOS $p = (\gamma - 1)\rho e - \gamma A, A = 6 \times 10^8$. The right material is ideal gases with EOS $p = (\gamma - 1)\rho e$. The interface is at $x_i = 0.7$ for the pure simulations, and is moved to $x_i = 0.7 + 0.5h$ for the mixed cell simulations. The problem is run to a final time of $t = 2.2 \times 10^{-4}$. The two initial states are

$$(v, \rho, p, \gamma) = \begin{cases} (0, 10^3, 10^9, 4.4) & \text{if } x < x_i \text{ (Material \#1)}, \\ (0, 50, 10^5, 1.4) & \text{if } x > x_i \text{ (Material \#2)}. \end{cases}$$

To confirm that the current closure model is consistent with the previously presented results [6, 5, 10], we perform a Q_1Q_0 simulation on 500 cells. In this case, for the mixed simulation, closure model is evaluated at one quadrature point. The final total pressure, density and specific internal energy from the mixed simulation are shown on Figure 7. Figure 8 shows the time evolution of the mixed cell for the material specific pressures, indicator functions, densities and specific internal energies. The plot compares the pure cells simulation to the mixed cell simulation. All fields behave as expected.

Next a Q_3Q_2 test is performed on 100 cells. The closure model is evaluated at 5 distinct quadrature points within the mixed cell. Figure 9 tracks time evolution around the interface for both Q_3Q_2 pure and mixed cell simulations. This plot compares (i) the left-most, middle, and right-most quadrature points of the mixed cell to the (ii) closest to the interface quadrature points of the pure cells. From

DOI: 10.1002/fld

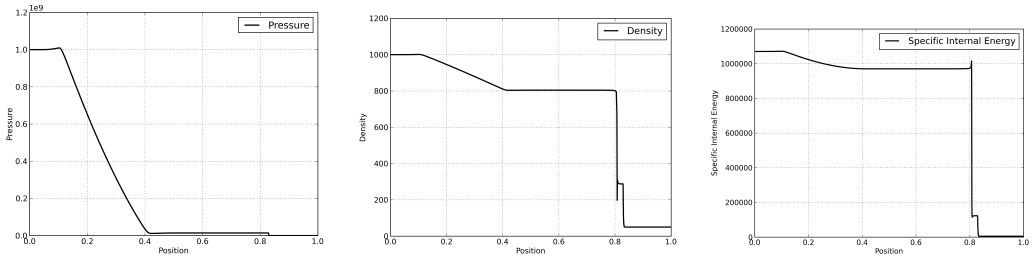

Figure 7. Total pressure, density and specific internal energy at $t = 2.2 \times 10^{-4}$ for the water-air shock tube test.

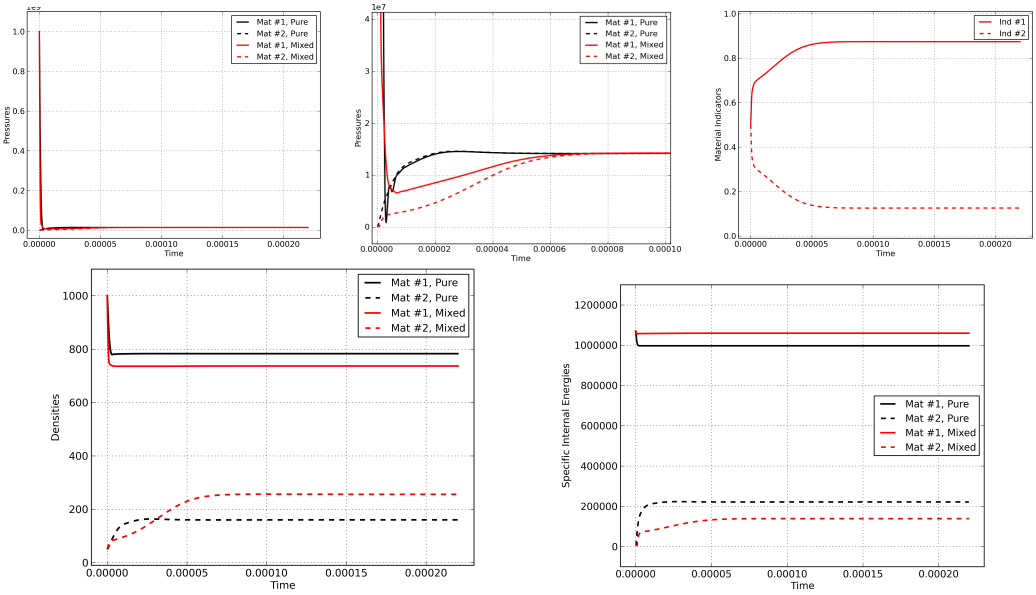

Figure 8. Time evolution of the mixed point for the Q_1Q_0 water-air shock tube test.

the zoomed pressure plot one can see that both pure and mixed simulations are more oscillatory compared to the Q_1Q_0 case, however equilibration is achieved at all points. The material indicators behave correctly as the water pushes away the air. Similar to the Sod tube problem, the initial spike in the left-most point does not cause a big spike in the air's specific internal energy.

6.4. 2D Gas Impact

This is a simplified high velocity impact problem introduced in [10]. There are three materials that represent an impactor, a wall and the background. All materials are ideal gases with EOS $p = (\gamma - 1)\rho e$, but they have different γ constants and densities. An ALE simulation is required in order to run to completion. This problem tests the ability of the presented closure model to work in 2D with three materials, and to couple with the ALE phase of our high-order finite element approach. Performing this simulation with Lagrangian indicators, i.e., $\Delta\eta_k = 0$, results in non-physical sound speeds and the computation fails, because the time step becomes too small.

The domain is $[0, 2] \times [0, 2]$ with $v \cdot n = 0$ boundary conditions. The material regions are $0.05 \leq x \leq 0.55$ and $0.9 \leq y \leq 1.1$ for the Impactor, $0.8 \leq x \leq 0.9$ for the Wall, and the rest is Background.

DOI: 10.1002/fld

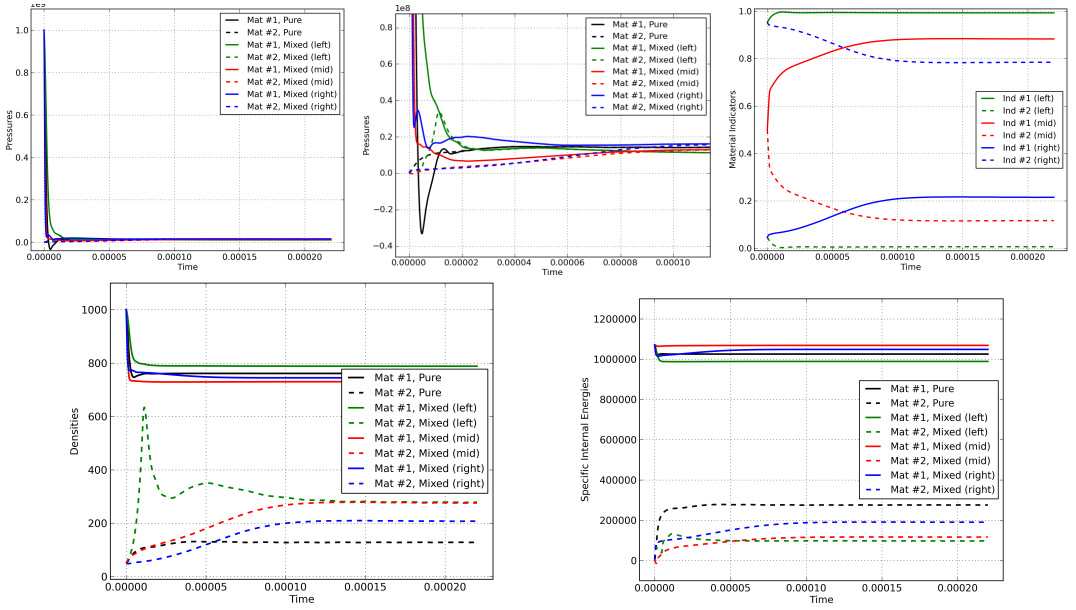

Figure 9. Time evolution of the mixed points for the Q_3Q_2 water-air shock tube test.

The problem is run to a final time of $t = 10$. The three initial states are

$$(v_x, v_y, \rho, p, \gamma) = \begin{cases} (0.2, 0, 20, 2, 50) & \text{if } x \in \text{ Impactor}\,, \\ (0, 0, 15, 1, 5/3) & \text{if } x \in \text{ Wall}\,, \\ (0, 0, 1, 1, 1.4) & \text{if } x \in \text{ Background}\,. \end{cases}$$

Presented is a Q_2Q_1 simulation on 160×160 cells. Every 20 Lagrange steps are followed by a remesh/ remap step. The remesh step resets the mesh to its original state. During the Lagrange steps, the closure model is evaluated at 16 distinct quadrature points within each mixed cell. During remap, and for visualization, the material indicators are represented as Q_2 finite element functions. Figure 10 shows the total density at different times during the simulation. Zoom of the impactor's material indicator function at final time are shown on Figure 11. The indicator functions transition smoothly and we do not observe material fragmentation, even after substantial deformation. This robustness can be explained by the fact that both the Lagrangian and remap phases of our high-order finite element approach are exclusively PDE-based, and interface reconstruction [17, 18] is not performed at any point of the calculation.

6.5. 3D Steel Ball Impact

As a final example, we consider a full 3D calculation of the high velocity impact of a steel ball against an aluminum plate. The configuration for this problem is adapted from the 2D test described in [19]. Here we consider a spherical steel projectile of radius 5.5 and initial velocity in the z-direction of $0.31cm/\mu s$ impacting a cylindrical plate of aluminum with a radius of 24 and a thickness of 2.5. Both the steel and aluminum materials use a Gruneisen equation of state combined with an elastic perfectly plastic "strength" model as described in [20]. The steel ball has an initial density of 7.81, a constant shear modulus of 0.770 Mbar and a constant yield stress of 3.4×10^{-4} Mbar

DOI: 10.1002/fld

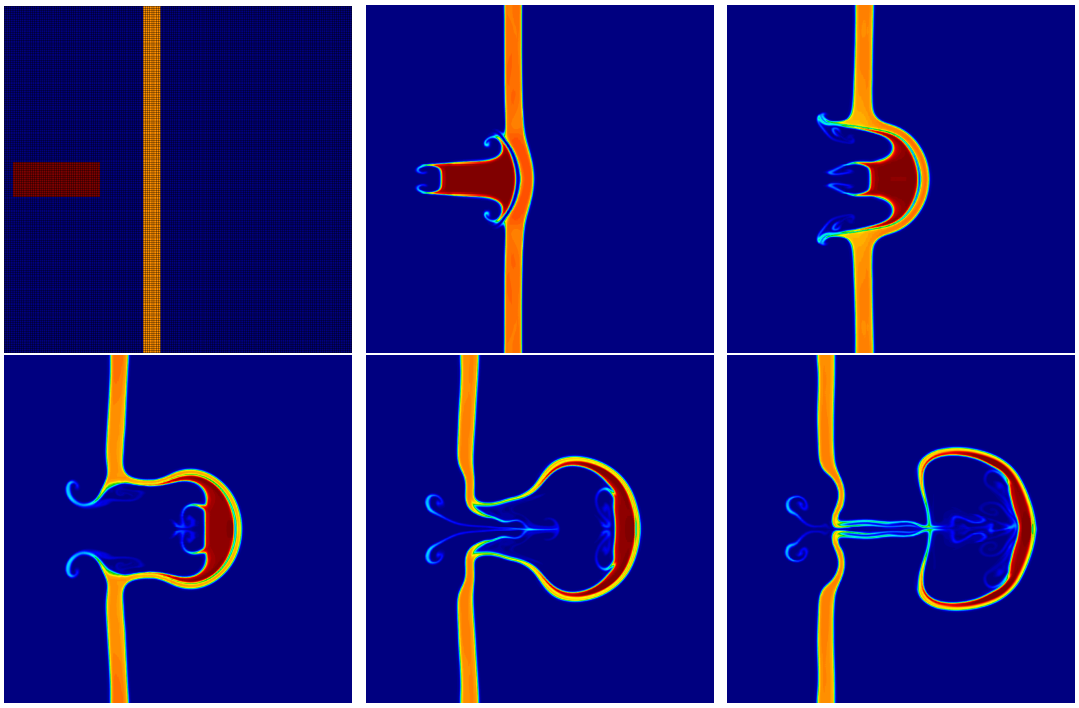

Figure 10. Total density profiles at times 0, 2, 4, 6, 8 and 10 for the 2D gas impact test.

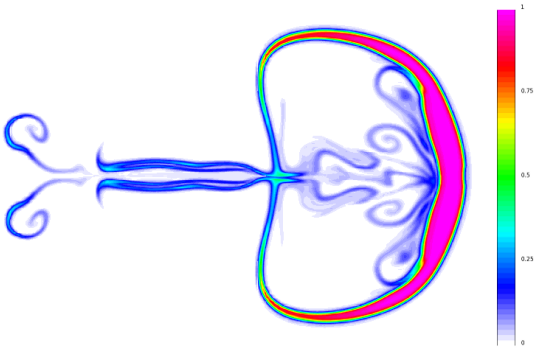

Figure 11. Material indicator function of the impactor at final time for the 2D gas impact test.

while the aluminum plate has an initial density of 2.7, a constant shear modulus of 0.271 Mbar and a constant yield stress of 4.0×10^{-4} Mbar. The steel and aluminum are separated by an air region which uses an ideal gas equation of state with an initial density of 0.001 and a constant adiabatic index $\gamma = 1.2$.

This problem tests the ability of the presented closure model to work in 3D with three materials including elastic-plastic material deformation models. In this case, the problem is run using a Q_2Q_1 method in an Eulerian-like fashion where the computational mesh is evolved purely Lagrangian for every 20 cycles, followed by a remap to the initial mesh. Figure 12 shows the total density and computational mesh at different times during the simulation. Figure 13 shows the "material" field which is computed as the sum of the material indicators weighted by the material number (e.g. material 1 corresponds to the air, 2 to the steel ball and 3 to the aluminum plate). As before, the materials transition smoothly and there are no fragments of material breaking free.

Prepared using fldauth.cls
DOI: 10.1002/fld

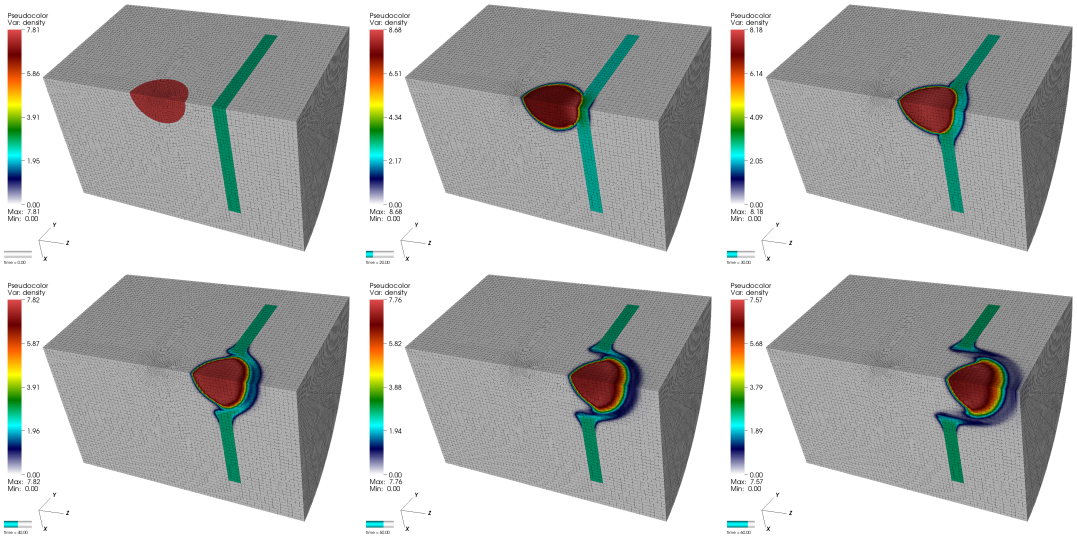

Figure 12. Total density profiles at times 0, 20, 30, 40, 50 and 60 for the 3D steel ball impact test.

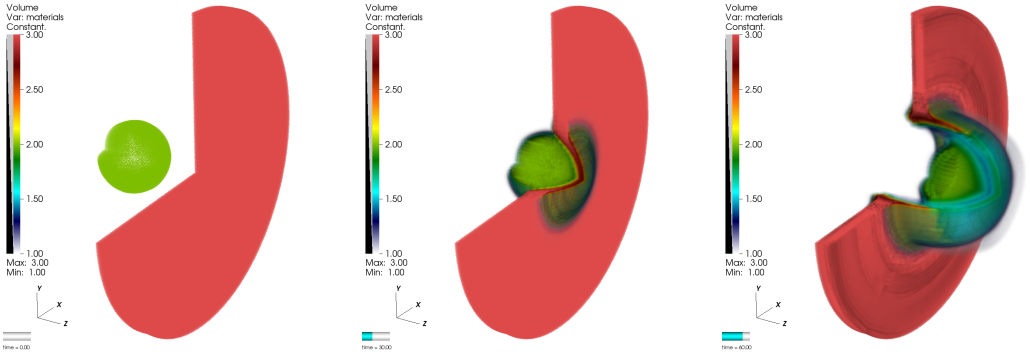

Figure 13. Material indicator functions of the impactor and plate at times 0, 30, and 60 for the 3D steel ball impact test.

7. CONCLUSION

We have presented a new closure model for multi-material Lagrangian hydrodynamics and its application to high-order finite element methods. The presented results indicate that the method deals robustly with sub-cell interactions in any dimension, for different types of materials, and for different polynomial spaces. The robustness of the method is further validated by the fact that all tests are performed with fixed parameters c_L and c_τ.

ACKNOWLEDGEMENTS

The authors would like to acknowledge the help of Robert Tipton, Douglas Miller, Tom Brunner and Robert Anderson of LLNL, whose guidance and input was very influential in the development of this paper. This work performed under the auspices of the U.S. Department of Energy by Lawrence Livermore National Laboratory under Contract DE-AC52-07NA27344, LLNL-JRNL-680774.

DOI: 10.1002/fld

REFERENCES

1. Dobrev VA, Kolev TV, Rieben RN. High-order curvilinear finite element methods for Lagrangian hydrodynamics. *SIAM J. Sci. Comp.* 2012; **34**(5):B606–B641. 1, 2, 3, 4, 10, 12
2. Tipton R. CALE Lagrange step. *Technical Report*, Lawrence Livermore National Laboratory October 1990. Unpublished. 1, 2
3. Hirt CW, Amsden AA, Cook JL. An arbitrary Lagrangian-Eulerian computing method for all flow speeds. *J. Comput. Phys.* 1974; **14**:277–253. 1
4. Miller D, Zimmermam G. An algorithm for time evolving volume fractions in mixed zones in Lagrangian hydrodynamics calculations. *Russian J. of Phys. Chem. B, Focus on Physics* 2009; **3**(1):117–121. 2, 5
5. Yanilkin Y, Goncharov E, Kolobyanin V, Sadchikov V, Kamm JR, Shashkov MJ, Rider WJ. Multi-material pressure relaxation methods for Lagrangian hydrodynamics. *Computers & Fluids* 2013; **83**:137 – 143. 2, 13, 15
6. Kamm JR, Shashkov MJ, Fung J, Harrison AK, Canfield TR. A comparative study of various pressure relaxation closure models for one-dimensional two-material Lagrangian hydrodynamics. *Internat. J. Numer. Methods Fluids* 2011; **65**:1311–1324. 2, 13, 15
7. Barlow A, Hill R, Shashkov MJ. Constrained optimization framework for interface-aware sub-scale dynamics closure model for multimaterial cells in Lagrangian and arbitrary Lagrangian-Eulerian hydrodynamics. *Technical Report LAUR-13-26180*, Los Alamos National Laboratory 2013. 2
8. Bondarenko Y, Yanilkin Y. Thermodynamic parameters simulation of mixed cells in gas dynamics. *Mat. Model.* 2002; **14**(6):63–81. 2
9. Després B, Lagoutière F. Numerical resolution of a two-component compressible fluid model with interfaces. *Progress in Computational Fluid Dynamics, an International Journal* 2007; **7**(6):295–310. 2, 13
10. Barlow A, Hill R, Shashkov MJ. Constrained optimization framework for interface-aware sub-scale dynamics closure model for multimaterial cells in Lagrangian and arbitrary Lagrangian-Eulerian hydrodynamics. *J. Comput. Phys.* 2014; **276**(0):92–135. 2, 7, 10, 13, 15, 16
11. Kamm JR, Shashkov MJ. A pressure relaxation closure model for one-dimensional, two-material Lagrangian hydrodynamics based on Riemann problem. *Commun. Comput. Phys.* 2010; **7**(5):927–976. 2
12. Sun M. A thermodynamic and dynamic subgrid closure model for two-material cells. *Internat. J. Numer. Methods Fluids* 2013; **73**(2):130–151. 2, 13
13. Guermond JL, Popov B, Tomov V. Entropy-viscosity method for the single material Euler equations in Lagrangian frame. *Comput. Methods Appl. Mech. Engrg.* 2016; **300**:402 – 426. 2
14. BLAST: High-order curvilinear finite elements for shock hydrodynamics. http://www.llnl.gov/CASC/blast. 12
15. Barlow A. A new Lagrangian scheme for multimaterial cells. *Proceedings of European Congress on Computational Methods in Applied Sciences and Engineering, ECCOMAS Computational Fluid Dynamics Conference*, Wales, U.K., 2001; 235–294. 13
16. Shashkov MJ. Closure models for multimaterial cells in arbitrary Lagrangian-Eulerian hydrocodes. *Internat. J. Numer. Methods Fluids* 2008; **56**(8):1497–1504. 13
17. Kuchařík M, Garimella RV, Schofield SP, Shashkov MJ. A comparative study of interface reconstruction methods for multi-material ALE simulations. *J. Comput. Phys.* 2010; **229**(7):2432–2452. 17
18. Kuchařík M, Shashkov MJ. Conservative multi-material remap for staggered multi-material arbitrary LagrangianEulerian methods. *J. Comput. Phys.* 2014; **258**:268–304. 17
19. Howell BP, Ball GJ. A free-Lagrange augmented Godunov method for the simulation of elastic-plastic solids. *J. Comput. Phys.* 2002; **175**:128–167. 17
20. Dobrev VA, Kolev TV, Rieben RN. High-order curvilinear finite elements for elastic-plastic Lagrangian dynamics. *J. Comput. Phys.* 2014; **257**(B):1062–1080. 17

DOI: 10.1002/fld